Supporting Information

High-performance Ultracapacitor Electrodes Realized by 3-dimensionally Bicontinuous Block Copolymer Nanostructures with Enhanced Ion Kinetics

Gun Ho Lee,[a] Byung Jun Park,[a,b] Tae Won Nam,[a] Ye Ji Kim,[a,c] Gyu Rac Lee,[a] Eugene N. Cho,[a,d] and Yeon Sik Jung[a,d*]

[a] Department of Materials Science and Engineering, Korea Advanced Institute of Science and Technology (KAIST), 291 Daehak-ro, Yuseong-gu, Daejeon 34141, Republic of Korea

[b] KEPCO Research Institute, 105 Munji-ro, Jeonmin-dong, Yuseong-gu, Daejeon 34056, Republic of Korea

[c] Department of Materials Science and Engineering, Massachusetts Institute of Technology, Cambridge, Massachusetts 02139, United States

[d] KAIST Institute for NanoCentury, Korea Advanced Institute of Science and Technology (KAIST), 291 Daehak-ro, Yuseong-gu, Daejeon 34141, Republic of Korea

Experimental Methods

Materials: All materials were used as purchased. Poly(styrene-*b*-vinylpyridine) (PS-*b*-PVP) polymers with number average molecular weights M_n = 30-*b*-8.5, 37-*b*-10.5, 58-*b*-16.5, 183-*b*-52 kg mol^{-1} were obtained from Polymer Source, Inc. Resorcinol ($\geq$ 99.0%), formaldehyde (37 wt%), and *N,N'*-Dimethylformamide (DMF, anhydrous, 99.8%) were obtained from Sigma Aldrich and stored in a dry atmosphere. A stainless steel (SUS304) foil current collector was obtained from Wellcos Corp.

Electrode Preparation: BCPs and resorcinol were mixed to a weight ratio of 10:3. The mixture was dissolved in DMF to solutions of 30 wt% for SVP-30, 25 wt% for SVP-50 and SVP-70, and 15 wt% for SVP-100, in order to maintain equivalent viscosity between solutions. The solutions were stirred at 300 rpm for 6 hours on a hotplate at 100 $^{\circ}$C, cooled to room temperature, and casted onto SUS304 stainless steel current collectors using the bar-coating technique. The bar-coatings were carried out using an automated film coating device (MRX-TMDH150) with its platform set at 25 $^{\circ}$C and coating speed set at 5 cm s^{-1}. The films were dried under ambient conditions for 30 minutes, followed by 2 hours in a vacuum chamber set at 60 $^{\circ}$C. The films were placed in DMF annealing chambers for 6 hours to induce self-assemblies and completely dried on a hotplate at 60 $^{\circ}$C for 1 hour. The self-assembled BCP films were then exposed to formaldehyde vapor at 100 $^{\circ}$C for 4 hours for resorcinol-formaldehyde (RF) resin formation. The films were then carbonized in a tube furnace filled with argon (99.999% purity) flowing at 1 L min^{-1} and heated to 700 $^{\circ}$C at a ramp of 5 $^{\circ}$C min^{-1} and maintained for 4 hours.

Physicochemical Characterizations: Specific surface areas were measured with the N_2 adsorption isotherm at 77 K on a Micromeritics 3Flex instrument. The nanostructures were degassed at 300 $^{\circ}$C for more than 8 hours prior to measurement, and the SSA values were

calculated using the Brunauer-Emmett-Teller method. The nanostructure morphologies were characterized using a field emission scanning electron microscope (FE-SEM, Hitachi S-4800). Average channel diameter and strut widths were evaluated from the SEM images. The arithmetic means, standard deviations, and standard errors of the respective dimensions are exhibited in Table S1.

Element compositions were measured with an elemental analyzer (Thermo Fisher Scientific FlashSmart), and their chemical states were examined with X-ray photoelectron spectroscopy (XPS, Thermo Fisher Scientific K-alpha). Graphitization of carbon was inspected with a Dispersive Raman Spectrometer (Horiba ARAMIS) using a 514 nm Ar laser. The electrical conductivities were compared by preparing 10-μm-thick nanostructures on quartz substrates and evaluating them in a vacuum probe station (MSTech M5VC). The electrolyte wettability was evaluated using a contact angle analyzer (SEO Phoenix) with a 6M KOH solution. Images were captured every 250 ms to observe the change in drop shape over time.

Electrochemical Characterizations: The electrochemical characteristics were analyzed with an electrochemical workstation (WonaTech ZIVE SP1). Capacitive performance was evaluated using CV and GCD curves measured in three-electrode and symmetric coin cell (two-electrode) configurations (Figure 3f) with 6M KOH aqueous electrolyte. In the three-electrode systems, the working electrode was held using a platinum electrode holder, while platinum coil and Ag/AgCl electrode were used as counter and reference electrodes, respectively. Potential windows for CV and GCD in the 3E configuration were from -0.9 to 0.1 V and from 0 to 1 V vs. Ag/AgCl, respectively. The symmetric coin cell configuration was assembled in coin-type CR2032 cells with electrodes punched into circles with diameter of 13mm and kept apart by a cellulose separator. Potential windows for CV and GCD in the coin cell configuration were both from 0 to 1 V vs. Ag/AgCl. For reliability, the capacitance values were averaged between

results from five out of seven samples, with the highest and lowest outliers omitted. Self-discharge performance was evaluated in the symmetrical coin cell configuration. The self-discharge curves were obtained by recording the open-circuit voltage for 24 hours after charging the electrodes at current density of 0.1 A g^{-1} to 1 V vs. Ag/AgCl and holding the potential for 1 hour.

Gravimetric capacitances were calculated from CV curves using the following equation:

$$C_S = \frac{\int_{V1}^{V2} IdV}{(V_2 - V_1) \cdot \Delta m \cdot v} \qquad (1)$$

where $\int_{V1}^{V2} IdV$ is the integrated area under the CV curve, V_2 and V_1 are respectively the upper and lower limits of the potential window, Δm is the mass of the active material, and v is the scan rate.

Alternatively, gravimetric capacitances were also calculated from the discharge portion of GCD curves using the following equation:

$$C_S = \frac{4I\Delta t}{m\Delta V} \qquad (2)$$

where I is the discharge current, Δt is the discharge time, m is the total mass of active material, and ΔV is the potential window.

Electrochemical impedance spectroscopy (EIS) analyses were carried out in the 3E configuration, in a frequency range from 100 kHz to 0.1 Hz at the open circuit potential with an AC perturbation of 10 mV.

Cycle stability tests were conducted with GCD analyses in the coin cell configuration, with potential windows from 0 to 1 V at a current density of 20 A g^{-1} for 30,000 cycles.

The BET-area-normalized capacitances were calculated from the specific capacitances and BET surface areas using the following equation:

$$C_{BET} = \frac{C_S}{S_{BET}} \qquad (3)$$

where C_s is the specific capacitance and S_{BET} is the specific surface area calculated with BET methods.

Energy densities and power densities were calculated from GCD characterizations in the symmetric coin cell configuration using the following equations:

$$E = \frac{1}{8} C_s \Delta V^2 \tag{4}$$

$$P = \frac{E}{\Delta t} \tag{5}$$

where C_s is specific capacitance, ΔV is the potential window, and Δt is the discharge time.

The real capacitance (C') and imaginary capacitance (C'') values were calculated with impedance values obtained from EIS analyses using the following equations:

$$C'(\omega) = \frac{-Z''(\omega)}{\omega |Z(\omega)|^2} \tag{6}$$

$$C''(\omega) = \frac{Z'(\omega)}{\omega |Z(\omega)|^2} \tag{7}$$

where ω is the angular frequency and $Z(\omega)$, $Z'(\omega)$, and $Z''(\omega)$ are the impedance, real component of impedance, and imaginary component of impedance, respectively.

Table S1. The arithmetic means, standard deviations, and standard errors of channel diameters and strut widths measured in the fabricated electrodes.

|		SVP-30	SVP-50	SVP-70	SVP-100
Channels	Arithmetic Mean (nm)	34.6	48.1	68.5	104.5
	Standard Deviation (nm)	4.2	5.8	8.8	15.6
	Standard Error (nm)	0.4	0.6	0.9	1.6
Struts	Arithmetic Mean (nm)	17.1	23.6	36.4	56.3
	Standard Deviation (nm)	2.1	2.9	4.8	9.1
	Standard Error (nm)	0.2	0.3	0.5	0.9
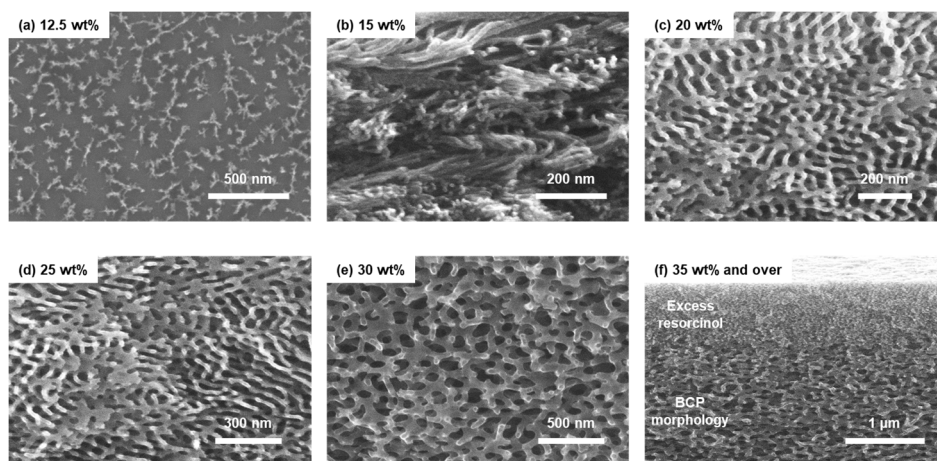
Figure S1. SEM Images of carbon nanostructures prepared with resorcinol compositions of (a) 12.5, (b) 15, (c) 20, (d) 25, (e) 30, and (f) 35 wt% of the PS-*b*-PVP.

As described above, resorcinol molecules were dissolved with PS-b-PVP and heated to form hydrogen bonds with the PVP blocks, followed by the carbonization process. Figure S1 shows that the BCP and RF resin mixtures successfully produced carbon nanostructures when the resorcinol composition was between 15 and 30 wt% of the PS-b-PVP. Samples prepared with less than 15 wt% resorcinol failed to maintain the 3D network upon carbonization (Figure S1a), presumably due to the insufficient amount of carbon precursor. On the other hand, samples with over 30 wt% resorcinol formed solid carbon layers on top of the 3D nanostructure (Figure S1f) due to the excess resorcinol molecules that were not able to bond with the PVP blocks. Accordingly, the absence of a carbon crust in samples with lower resorcinol compositions (Figures S1b to S1e) indicated that the added resorcinol monomers were completely integrated into the PVP chains.

Additionally, the selective incorporation led to an increase in the relative volume fraction of the PVP domain with respect to the amount of the resorcinol added to the solution. The changes in relative volume fractions were distinct in the self-assembled morphologies. Figure S1e shows the 3D morphology of the nanostructures used in this study, prepared with 30 wt% resorcinol. On the other hand, the nanostructures prepared with smaller resorcinol compositions

(Figures S1b to S1d) exhibited a randomly arranged mixture of perforated lamellae and cylinders. The cylindrical morphology became more dominant as the resorcinol composition decreased, indicating a reduction in the relative volume fractions of the PVP domains. Comparison of the self-assembled morphologies displayed the alterations in the relative volume fraction due to the selective incorporation of resorcinol monomers.
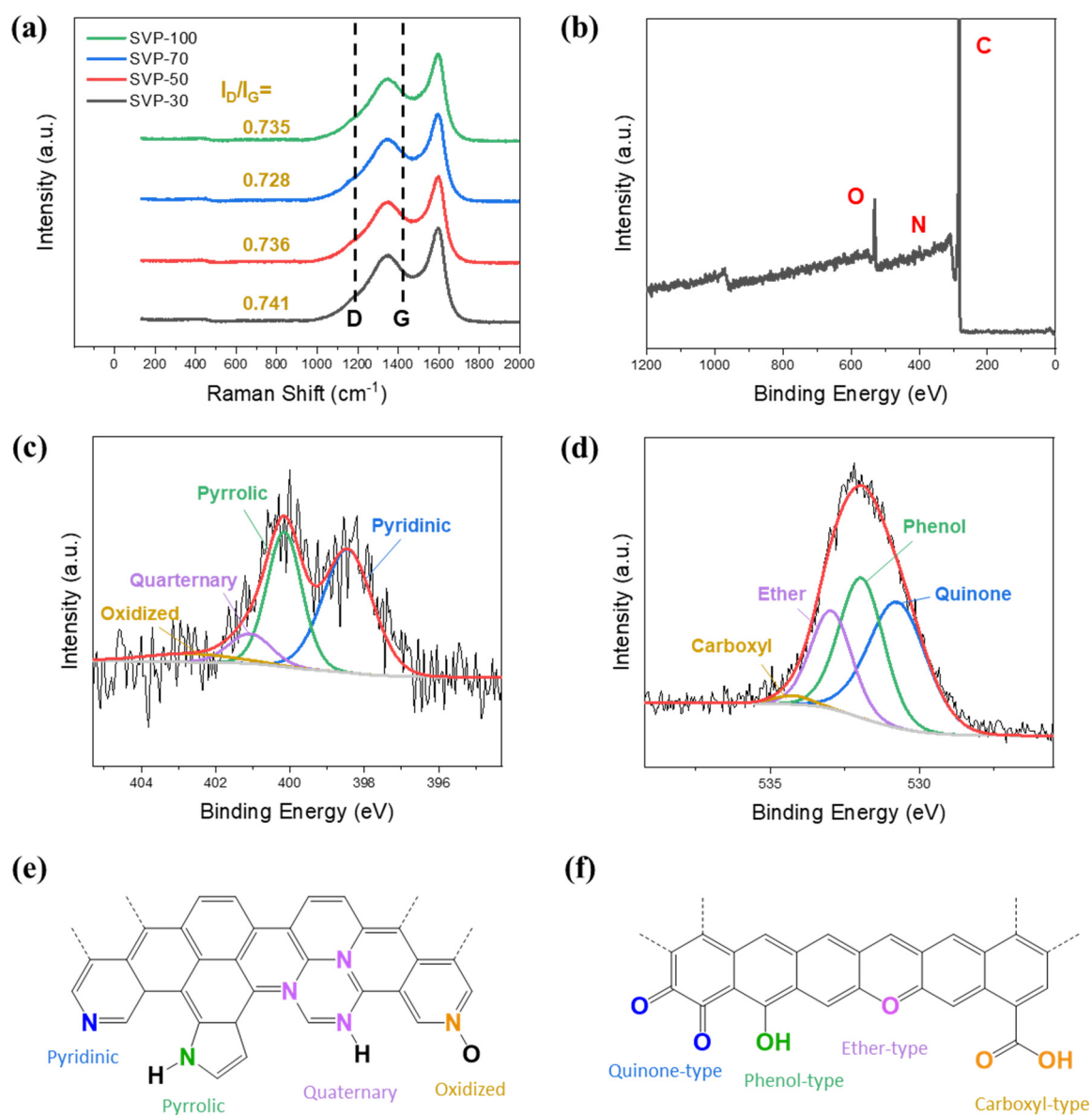
Figure S2. Raman spectra and XPS results. (a) Raman spectra of four electrodes with carbon peaks at 1350 cm^{-1} (D band) and 1600 cm^{-1} (G band). (b) XPS spectra and deconvolutions of (c) N 1s peak and (d) O 1s peak. Schematics of (e) the nitrogen functionalities and (f) the oxygen functionalities.

Table S2. Relative compositions of nitrogen and oxygen functional groups calculated from deconvolution of N 1s and O 1s XPS spectra.

N functional groups			O functional groups		
Species	Binding Energy (eV)	Content (at.%)	Species	Binding Energy (eV)	Content (at.%)
Pyridinic N	398.5 eV	47.54	Quinone-type O	530.7 eV	40.81
Pyrrolic N	400.2 eV	36.72	Phenol-type O	531.9 eV	34.93
Quarternary N	401.1 eV	9.85	Ether-type O	533.0 eV	22.44
Oxidized N	402.7 eV	5.89	Carboxyl-type O	534.2 eV	1.82

Table S3. Elemental analysis results of the fabricated electrodes.

Electrodes	Carbon (at.%)	Nitrogen (at.%)	Oxygen (at.%)
SVP-30	92.48	2.24	5.27
SVP-50	91.16	2.67	6.17
SVP-70	91.34	2.63	6.03
SVP-100	91.66	2.58	5.76
Average	91.66	2.53	5.81

Raman Spectroscopy

The G band (1600 cm^{-1}) and D band (1350 cm^{-1}) peaks from the Raman spectra in Figure S2a were used to compare the degrees of structural order in the carbons. The G peak of carbon is derived from vibrations in sp^2-bonded crystalline carbon and reflects the structural order in crystalline components in carbonaceous materials.[1] The full width at half maximum (FWHM) of the peak is generally known to reflect the crystallinity in carbon.[2,3] The four electrodes exhibited FWHM values of 80.79, 79.41, 78.33, and 81.66 cm^{-1}, respectively, for SVP-30,

SVP-50, SVP-70, and SVP-100. The comparable FWHM values indicated similar crystallinities in all four electrodes.

Ratios of the intensities of the two peaks, or I_D/I_G ratios, are commonly used to characterize the level of disorder in graphitic carbons. The four electrodes exhibited analogous I_D/I_G ratios of 0.735, 0.728, 0.736, and 0.741, respectively, for SVP-30, SVP-50, SVP-70, and SVP-100. The low average value of 0.73 validated the formation of well graphitized carbon nanostructures for all four samples. Furthermore, the crystallite sizes (L_a) in carbonaceous materials are inversely proportional to the intensity ratio and can be estimated using the following equation[4,5]:

$$L_a = \frac{560}{E_l{}^4}\left(\frac{I_D}{I_G}\right)^{-1}$$

where E_l is the excitation laser energy used in the Raman spectroscopy. The inverse correlation between the L_a and I_D/I_G ratios and the comparable intensity ratios observed in the samples indicated that the four nanostructures have similarly sized crystallites.

X-ray Photoelectron Spectroscopy

Nearly identical XPS results were acquired from all four samples. The spectrum obtained from SVP-100 is demonstrated as an example in Figures S2b to S2d. Figure S1b reveals the presence of carbon, nitrogen, and oxygen in the electrodes. Deconvolutions of the high-resolution XPS peaks, presented in Figures S2c and S2d, identified pyridinic nitrogen, pyrrolic nitrogen, and quinone-type oxygen as the dominant functionalities, as listed in Table S2. These heteroatom dopant types are reported to be electrochemically active sites with pseudocapacitive redox reactions in an alkaline electrolyte.

Electrical Conductivity

Electrical conductivities of the carbon nanostructures were compared using a probe station. The electrodes were prepared on insulating quartz substrates, and the electrical conductivities of the carbon structures were evaluated from current-voltage (I-V) curves obtained in the potential range from -5 to 5 V. The four electrodes demonstrated comparable conductivity values of 3.63, 3.75, 3.83, and 3.96 S cm^{-1} for SVP-30, SVP-50, SVP-70, and SVP-100, respectively. The slightly greater conductivities in the nanostructures having larger dimensions correspond to the EIS analysis results and are ascribed to the enhanced conductivities due to the larger struts.

The analyses revealed analogous physicochemical properties in the four electrodes, which was to be expected as the samples were fabricated from chemically identical precursors. These results validate that the differences in capacitive performance of the electrodes derived mostly from their structural distinctions, not from their physical and chemical attributes.
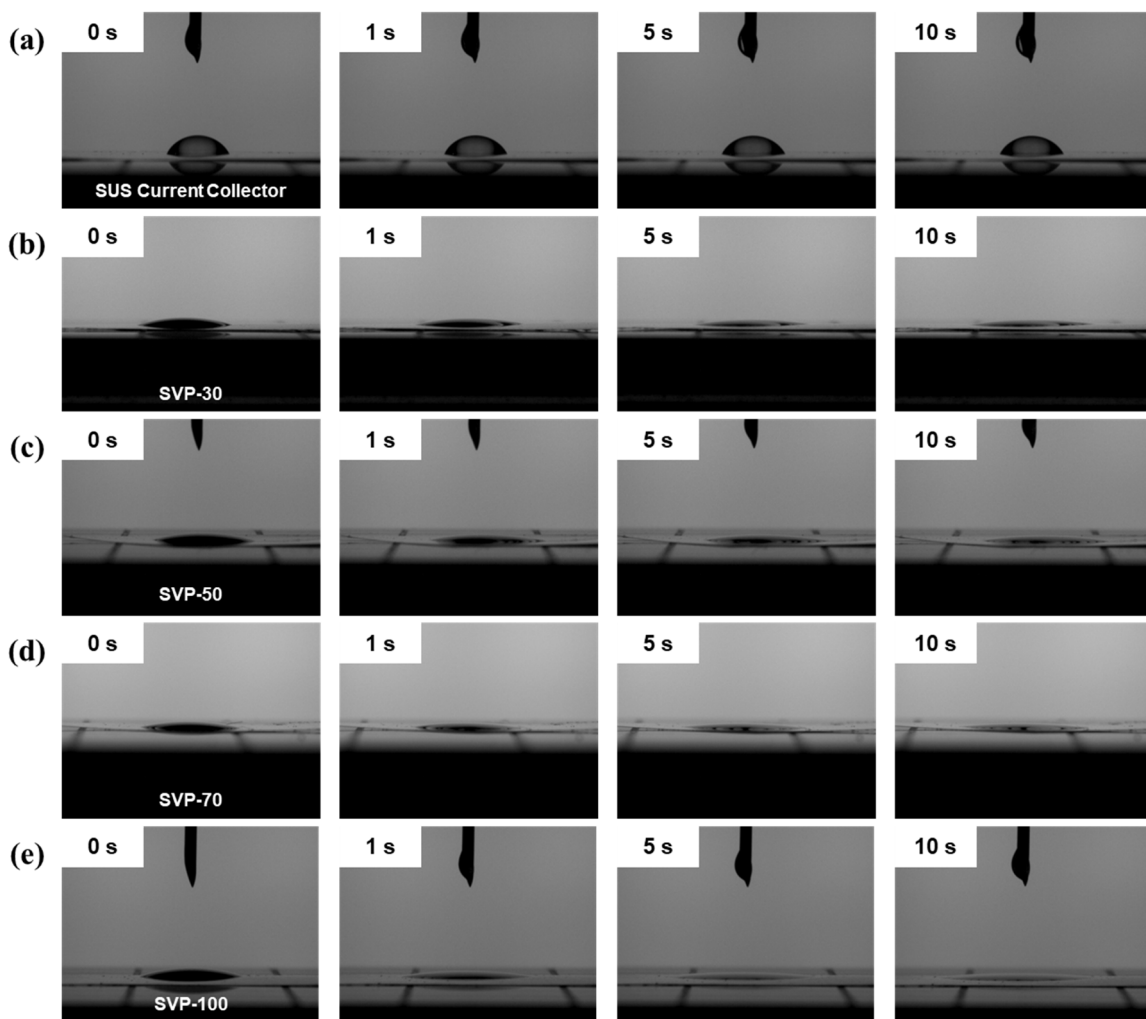
Figure S3. Wettability analysis with images captured 0, 1, 5, and 10 seconds after the point of contact. 6M KOH dropped on (a) SUS current collector without the carbon nanostructures, (b) SVP-30, (c) SVP-50, (d) SVP-70, and (e) SVP-100.

The electrolyte wettabilities of the fabricated electrodes were evaluated using a contact angle analyzer with a 6M KOH electrolyte. As can be seen in Figure S3, the four samples showed exceptional wettabilities, especially compared to the bare SUS current collector without the carbon nanostructures (Figure S3a). As can be seen in the images captured as a function of time, the electrolyte was instantaneously absorbed into the electrodes after the deposition. The contact angles on the carbon nanostructures were roughly estimated (due to the

narrow angles) to be 15º at 0 s but were reduced to less than 5º at 10 s due to the absorption. Bare SUS, on the other hand, maintained the initial contact angle of 60º.

The electrodes demonstrated excellent wettabilities with the aqueous electrolyte despite the nanostructured surface. This is attributed to the highly interconnected channels in the three-dimensional porous carbon nanostructures and the wettability enhancement effect from the heteroatom dopants, which allows the solution to swiftly permeate the nanostructures. Among the four samples, SVP-100 showed the best wettability with the fastest electrolyte absorption, corresponding to its superior electrolyte kinetics and accessibility, as discussed in the study.
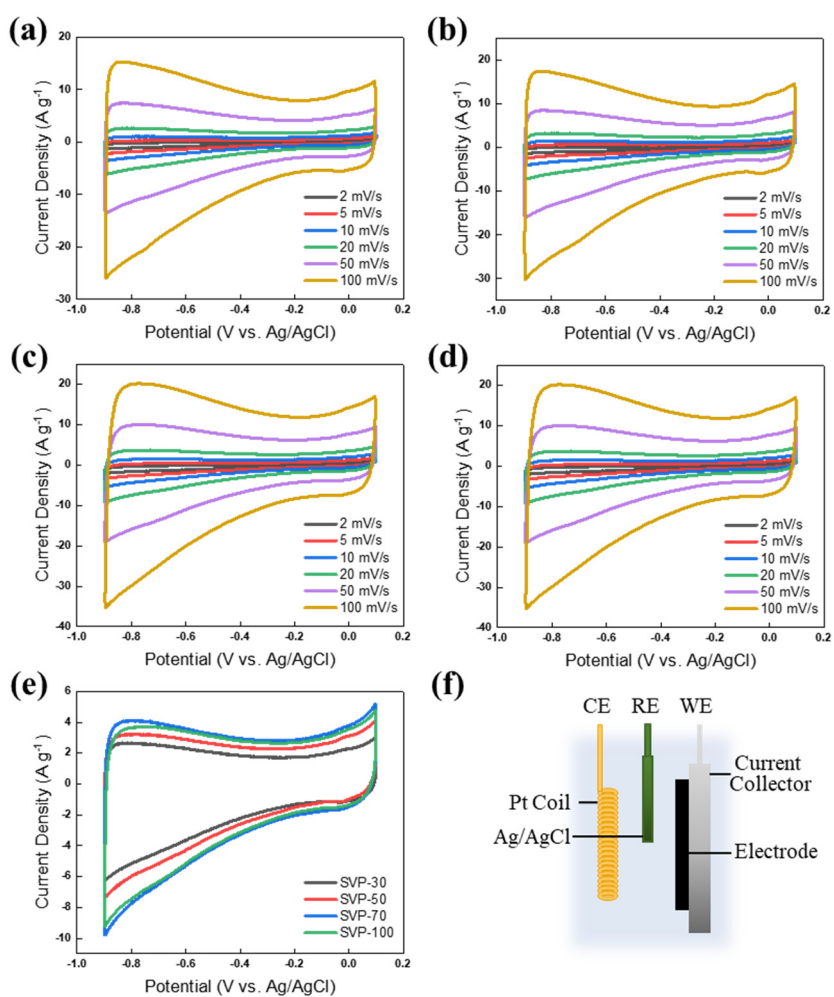
Figure S4. Cycle voltammetry characterizations in 3-electrode configuration. CV curves of (a) SVP-30, (b) SVP-50, (c) SVP-70, and (d) SVP-100 electrodes. (e) Comparison of curves measured at scan rate of 20 mV s^{-1}. (f) Schematic of 3-electrode configuration used in the evaluation.
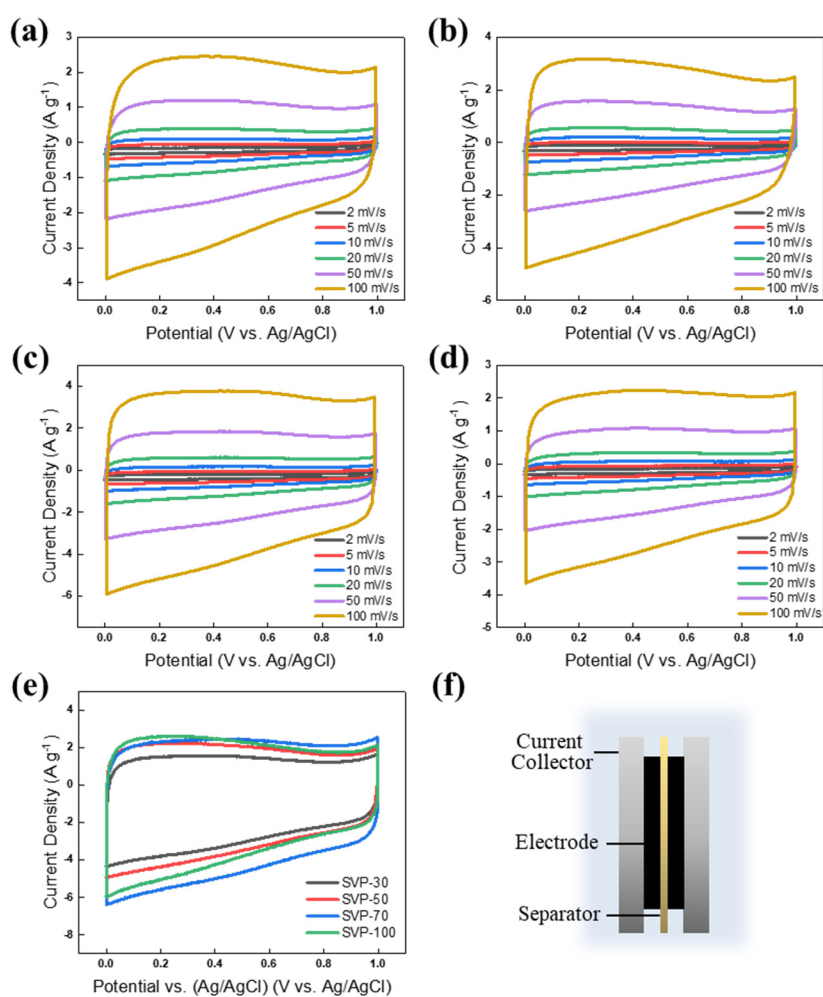
Figure S5. Cycle voltammetry characterizations in symmetric coin cell configuration. CV curves of (a) SVP-30, (b) SVP-50, (c) SVP-70, and (d) SVP-100 electrodes. (e) Comparison of curves measured at scan rate of 20 mV s^{-1}. (f) Schematic of symmetric coin cell configuration used in the evaluation.

Figures S4 and S5 show cycle voltammetry (CV) curves of the samples, obtained in 3-electrode and symmetric coin configurations, respectively. The curves are rectangular in shape with no discernable redox peaks in both configurations, indicating ideal capacitive behaviors. The CV curves of the four electrodes at a scan rate of 20 mV s^{-1} are directly compared in Figures S4e and S5e. The four electrodes show similarly shaped curves with slight differences in current density levels, indicating that all electrodes exhibit analogous electrochemical behaviors but with different capacities, as discussed in the article.

16
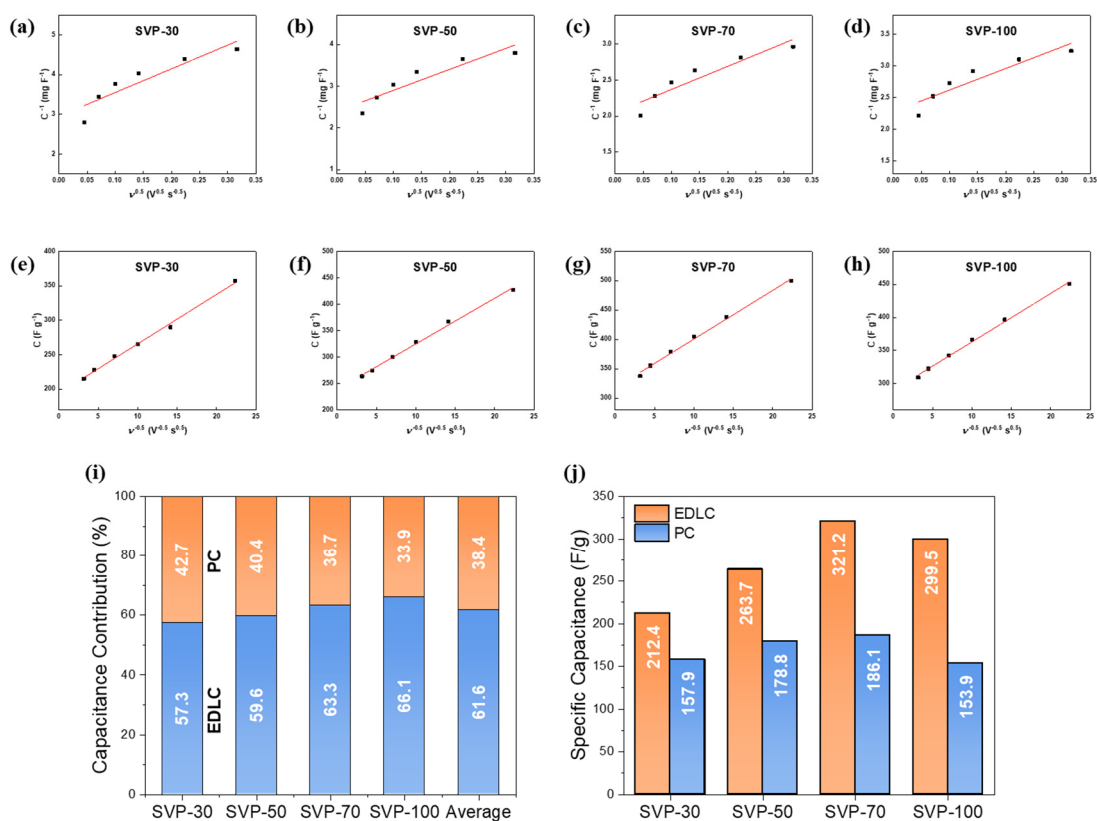
Figure S6. Trasatti analysis to differentiate EDLC and PC contributions in the fabricated electrodes. (a)-(d) Linear regression lines for C^{-1} plotted against $\upsilon^{0.5}$ and (e)-(h) linear regression lines for C plotted against $\upsilon^{-0.5}$. (i) (j) The calculated EDLC and PC proportions of the four electrodes.

Table S4. Trasatti analysis results for EDLC and PC contributions to specific capacitance.

	Total Specific Capacitance [F g^{-1}]	EDLC contribution [%]	Pseudocapacitance contribution [%]	EDLC contribution [F g^{-1}]	Pseudocapacitance contribution [F g^{-1}]
SVP-30	370.3	57.3	42.7	212.4	157.9
SVP-50	442.5	59.6	40.4	263.7	178.8
SVP-70	507.3	63.3	36.7	321.2	186.1
SVP-100	453.4	66.1	33.9	299.5	153.9
Average	443.4	61.6	38.4	274.2	169.2

The electrical double layer capacitance (EDLC) and pseudocapacitance (PC) of the fabricated electrodes were differentiated using an estimation technique first suggested by Trasatti et al.[6] Gravimetric capacitance values obtained from the four samples at scan rates ranging from 2 to 100 mV s^{-1} were used in the analyses. The total capacitance values of the electrodes (C_T) were first estimated by calculating the capacitance at $\upsilon \rightarrow 0$ by linear fitting of the reciprocal of the specific capacitance values (C^{-1}) and the square root of the scan rates ($\upsilon^{0.5}$), as shown in Figures S6a to S6d. The linear relationship can be described by the following equation[7]:

$$C^{-1} = \alpha \cdot \upsilon^{\frac{1}{2}} + C_T{}^{-1}$$

On the other hand, the EDLC contribution in the capacitive performance (C_{EDL}) can be calculated from the capacitance values (C) plotted against the reciprocal of the square root of scan rates ($\upsilon^{-0.5}$) in Figures S6e to S6h. The linear regression can be described by the following equation:

$$C = \beta \cdot \upsilon^{-\frac{1}{2}} + C_{EDL}$$

The PC contribution (C_P) can then be calculated by subtracting C_{EDL} from C_T.

The analyses results are shown in Figures S6i and S6j and Table S4. It must be noted that Trasatti's method of capacitance differentiation relies on the relationship between scan rates and specific capacitance values. Consequently, electrodes with superior rate capabilities exhibited greater EDLC proportions, as shown in Figure S6i. Nevertheless, analogous correlations between the capacitive performance and the channel dimensions were observed in both C_{EDL} and C_P of the four electrodes. Figure S6j demonstrates that the EDLC and PC values both increased with the channel size for SVP-30, SVP-50, and SVP-70, but a further increase in size scale resulted in a slight decrease for SVP-100. The average pseudocapacitive contributions were estimated as 38.4%.
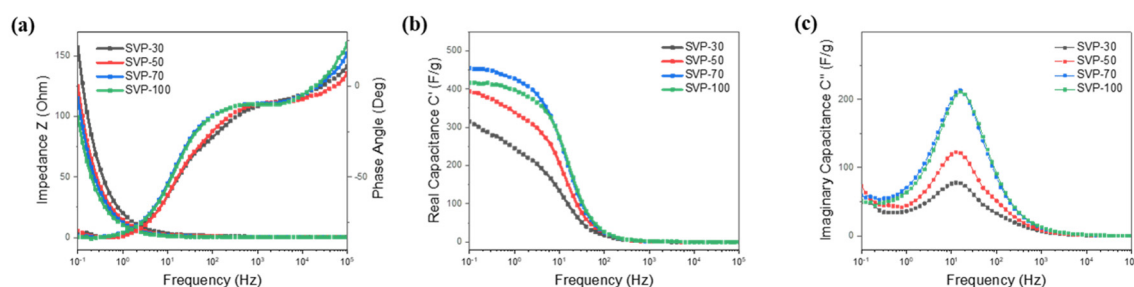
Figure S7. (a) Bode plot with impedance values and phase angles, (c) real capacitance, (d) and imaginary capacitance plotted against frequency.

Impedance and Phase Angles

Figure S7a presents Bode plots of the four samples with impedance and phase angles plotted against frequency, calculated from the impedance values obtained in the EIS analysis. The fabricated carbon nanostructures exhibited phase angles of over 80°, indicating excellent capacitive behaviors deriving from favorable ion charge transfer conditions at the electrode-electrolyte interface.[8,9]

Real and Imaginary Capacitance

The capacitance C of an electrode can be defined in terms of the real capacitance (C') and imaginary capacitance (C'') as follows:

$$C(\omega) = C'(\omega) - jC''(\omega)$$

The C' and C'' values at each frequency were calculated and are plotted in Figure S7b and S7c. The real capacitance C' reflects the actual delivery of the stored energy, while the imaginary capacitance C'' reveals the dissipation of the energy due to various losses in the system. As thoroughly discussed in the article, the C' curves demonstrated saturated capacitance values and superior rate capabilities of the electrodes with larger channels. The C'' curves, on the other hand, provided information on the discharge capabilities and consequentially the power densities of the electrodes. The knee frequency f_0, where C'' reaches

19

its maximum value, is inversely proportional to the relaxation time constant ($\tau_0 = \frac{1}{f_0}$).[10,11] τ_0 is defined as the minimum time required to deliver energy with an efficiency greater than 50% and reflects the swiftness of the discharge performance.[12] Therefore, higher knee frequency f_0 indicates greater discharge capability.[10] As seen in Figure S7c, the electrodes with larger structural dimensions exhibited greater knee frequencies, corresponding to their superior discharge capabilities demonstrated in their rate capability and power density performance. SVP-100 exhibited the lowest τ_0 value of 63.1 ms, validating the rapid discharge capabilities of the fabricated electrodes.
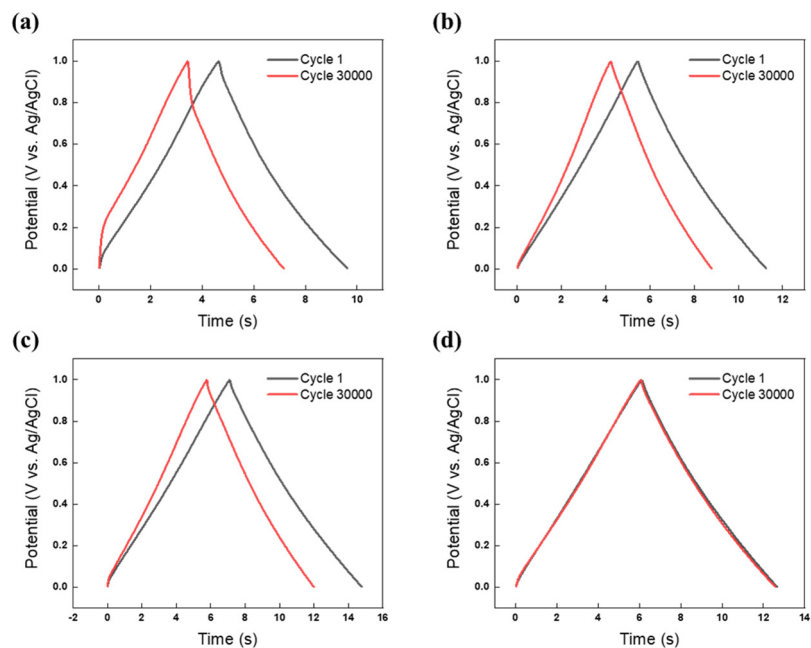
Figure S8. Galvanostatic charge-discharge characterizations of the four electrodes before and after cycle stability tests. (a) SVP-30, (b) SVP-50, (c) SVP-70, and (d) SVP-100 electrodes. All curves were measured at a current density of 20 A g^{-1}.

As mentioned in the paper, cycleability tests of the electrodes were conducted with 30,000 cycles of charging and discharging under a current density of 20 A g^{-1}. Figure S8 shows the galvanostatic charge-discharge (GCD) curves of the four electrodes recorded at the first and last cycles of the cycleability test. In Figure S8a, the GCD curves of the SVP-30 electrode show the most distortions after the cycle stability test, consistent with its low capacitance retention. The curves of both the SVP-50 and SVP-70 electrodes show reduced charging and discharging duration but maintain their triangular shape, as respectively shown in Figures S8b and S8c. The SVP-100 electrode, on the other hand, displays excellent stability with negligible changes in both the GCD curve and discharge duration (Figure S8d), corresponding to its exceptional cycle stability.
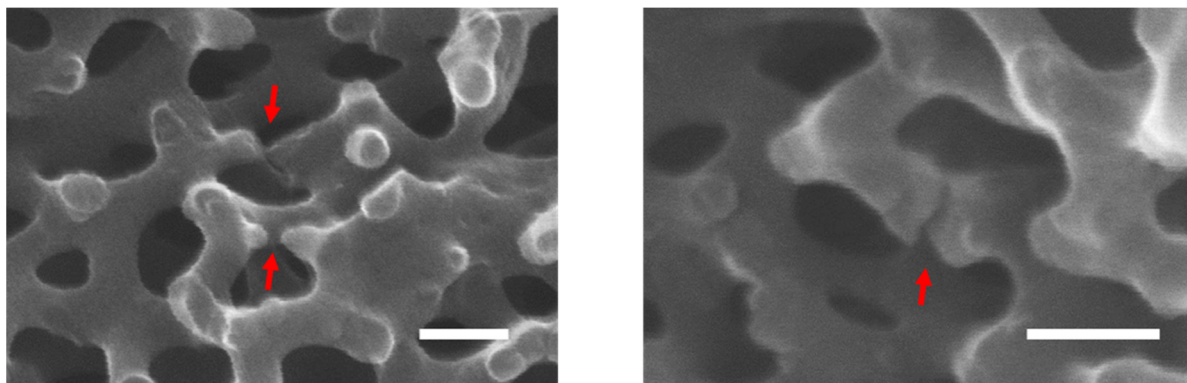
Figure S9. SEM images of the electrodes retrieved after the cycle stability tests. Scale bars indicate 100 nm.

Figure S9 shows the structural degradations observed in the carbon nanostructures retrieved after the durability tests of 30,000 cycles. The repeated cycles caused similar damage in all four electrodes, leading to disconnected struts, as marked in the SEM images with arrows. The outstanding cycleability results despite such critical deteriorations are attributed to the network structure of the 3D electrodes. The high connectivity of the bicontinuous nanostructures allows charges to detour and maintains the conductivity even after a fraction of the struts are severed, thus rendering the electrodes tolerant to partial disconnections in the structures. As discussed in the article, the disparities between the cycle stabilities observed in the four electrodes can be attributed to the differences in their strut radii. Thicker struts are more resistant to deterioration, and consequently the electrodes with larger dimensions are more tolerant to degradation and their cycle lives are extended.

Table S5. Summary of capacitive performance of mesoporous and macroporous nanostructures used in Figure 5.

	Article Title	Brief Description of the Structures	Specific Surface Area ($m^2\ g^{-1}$)	Specific Capacitance ($F\ g^{-1}$)	Area-normalized capacitance ($\mu F\ cm^{-2}$)	Macropore and Mesopore Size (nm)	References
1	Superior capacitive performance of active carbons derived from Enteromorpha prolifera	Hierarchical structure from E. prolifera	2283	296	13.0	4.0	X. Gao et al., Electrochim. Acta. 133, 459–466 (2014).
2	Hierarchical porous carbon derived from recycled waste filter paper as high-performance supercapacitor electrodes	Hierarchical activated porous carbon from recycled filters	2170	302.3	13.9	8.0	B. Chang, Y. Guo, Y. Li, B. Yang, RSC Adv. 5, 72019–72027 (2015).
3	Fabrication of porous carbon nanofibers with adjustable pore sizes as electrodes for supercapacitors	Porous carbon nanofibers	1614	210	13.0	4.7	C. Tran, V. Kalra, J. Power Sources. 235, 289–296 (2013).
4	Porous carbons prepared from deoiled asphalt and their electrochemical properties for supercapacitors	Porous carbon from deoiled asphalt	1778	302	17.0	3.9	W. Zhang, Z.-H. Huang, Z. Guo, C. Li, F. Kang, Mater. Lett. 64, 1868–1870 (2010).
5	Nanostructured mesoporous carbon as electrodes for supercapacitors	Mesoporous, nongraphitized carbon black	469	41.5	8.8	15	S. R. S. Prabaharan, R. Vimala, Z. Zainal, J. Power Sources. 161, 730–736 (2006).
6	Enhanced electrochemical performance for EDLC using ordered mesoporous carbons (CMK-3 and CMK-8): Role of mesopores and mesopore structures	Ordered mesoporous carbons (OMCs) with silica as templates	1064	78	7.3	4.4	T. N. Phan, M. K. Gong, R. Thangavel, Y. S. Lee, C. H. Ko, J. Alloys Compd. 780, 90–97 (2019).
7	Design and synthesis of three-dimensional hierarchical ordered porous carbons for supercapacitors	3D hierarchical porous carbons (HPCs) with silica nanosphere array as template	1182	243.5	20.6	8.0	Q. Zhao et al., Electrochim. Acta. 154, 110–118 (2015).
8			879	171.1	19.5	15.0	
9			782	194.2	24.8	30.0	
10	Mesopore-dominant activated carbon aerogels with high surface area for electric double-layer capacitor application	Mesoporous activated carbon aerogel	1417	161	11.4	20.0	C. Li, X. Yang, G. Zhang, Mater. Lett. 161, 538–541 (2015).
11	Synthesis of starch-derived mesoporous carbon for electric double layer capacitor	Starch-derived mesoporous spherical micelles	441	80	18.1	3.7	M. Wu et al., Chem. Eng. J. 245, 166–172 (2014).
12			1157	144	12.4	3.5	
13			841	89	10.6	3.4	
14	Layered graphene/mesoporous carbon heterostructures with improved mesopore accessibility for high performance capacitive deionization†	Layered graphene sheets and mesoporous carbons	1270	125.7	9.9	40.9	O. Noonan, Y. Liu, X. Huang, C. Yu, J. Mater. Chem. A. 6, 14272–14280 (2018).
15			1100	77	7.0	41.4	
16			924	75.5	8.2	51.3	
17			807	53.9	6.7	33.6	
18			1275	148	11.6	11.0	

19	Nitrogen and phosphorus co-doped cubic ordered mesoporous carbon as a supercapacitor electrode material with extraordinary cyclic stability	N and P co-doped OMCs	642.6	205	31.9	24.0	T. Panja, D. Bhattacharjya, J.-S. Yu, J. Mater. Chem. A. 3, 18001–18009 (2015).
20	Promising activated carbons derived from waste tea-leaves and their application in high performance supercapacitors electrodes	Activated carbon (ACs) from waste tea-leaves	2841	330	11.6	2.7	C. Peng et al., Electrochim. Acta. 87, 401–408 (2013).
21			2540	305	12.0	3.0	
22			2607	280	10.7	3.2	
23			2521	275	10.9	3.0	
24			950	66	6.9	5.1	
25	Highly mesoporous and high surface area carbon: A high capacitance electrode material for EDLCs with various electrolytes	AC fibers	3211	356	11.1	5	B. Xu et al., Electrochem. commun. 10, 795–797 (2008).
26			3291	371	11.3	5	
27			3001	337	11.2	5	
28			2839	330	11.6	5	
29	Synthesis of mesoporous carbon spheres with a hierarchical pore structure for the electrochemical double-layer capacitor	Hierarchically mesoporous carbon spheres	1321	208	15.7	60	Q. Li et al., Carbon N. Y. 49, 1248–1257 (2011).
30			901	146	16.2	26.0	
31	Characterization of the porous carbon prepared by using halloysite as template and its application to EDLC	Holloysite-derived nanostructure with nanoscale holes	1142	261	22.9	4.0	G. Liu, F. Kang, B. Li, Z. Huang, X. Chuan, J. Phys. Chem. Solids. 67, 1186–1189 (2006).
32	Electrochemical properties of mesoporous carbon aerogel electrodes for electric double layer capacitors	Mesoporous carbon aerogel	598	193.6	32.4	10.2	L. I. U. Ling, di, 4105–4107 (2005).
33			602	164.6	27.3	9.0	
34			729	202.2	27.7	8.7	
35			855	196.4	23.0	10.0	
36	Nitrogen-containing carbon spheres with very large uniform mesopores: The superior electrode materials for EDLC in organic electrolyte	Mesoporous carbon spheres	1460	159	10.9	31.0	W. Li et al., Carbon N. Y. 45, 1757–1763 (2007).
37	Hierarchical Microporous/Mesoporous Carbon Nanosheets for High-Performance Supercapacitors	Mesoporous carbon nanosheet	960	160 (approx.)	16.7	12.0	A. B. Fuertes, M. Sevilla, ACS Appl. Mater. Interfaces. 7, 4344–4353 (2015).
38			1630	165 (approx.)	10.1	20.0	
39			1890	190 (approx.)	10.1	30.0	
40	Nickel Nanofoam/Different Phases of Ordered Mesoporous Carbon Composite Electrodes for Superior Capacitive Energy Storage	OMCs with carbonized BCPs	479.62	199	41.5	30.0	K. Lee et al., ACS Appl. Mater. Interfaces. 8, 22516–22525 (2016).
41			856.76	262	30.6	20.0	
42			814.5	259	31.8	25.0	
43	Hierarchically porous carbon by activation of shiitake mushroom for capacitive energy storage	HPC particles	2988	306	10.2	8.0	P. Cheng et al., Carbon N. Y. 93, 315–324 (2015).
44	Macropore- and Micropore-Dominated Carbon Derived from Poly(vinyl alcohol) and Polyvinylpyrrolidone for	hiearchical carbon with macro- and micro-pores	1700	132	7.8	33.3	K. Tang et al., ACS Sustain. Chem. Eng. 5, 11324–11333 (2017).

|							
	Supercapacitor and Capacitive Deionization						
45	A novel synthesis of hierarchical porous carbons from interpenetrating polymer networks for high performance supercapacitor electrodes	HPCs from polymer networks	727	108	14.9	3.8	D. Zhu et al., Carbon N. Y. 111, 667–674 (2017).
46			1371	288	21.0	3.8	
47			976	218	22.3	3.8	
48	Simple synthesis of hierarchical porous carbon from Enteromorpha prolifera by a self-template method for supercapacitor electrodes	HPCs	2200.8	216.9	9.9	3.6	Y. Gao et al., J. Power Sources. 270, 403–410 (2014).
49	Phosphorus-doped 3D hierarchical porous carbon for high-performance supercapacitors: A balanced strategy for pore structure and chemical composition	Phosphorus-doped 3D HPCs	940	367	39.0	13.0	W. Yang et al., Carbon N. Y. 127, 557–567 (2018).
50	Supercapacitive performance of hierarchical porous carbon microspheres prepared by simple one-pot method	HPC microspheres	709	221	31.2	4.6	Q. Zhao et al., J. Power Sources. 254, 10–17 (2014).

Table S5 lists the electrochemical performance values of mesoporous carbon electrodes reported in the literature, which are used in plotting the charts in Figure 5. There are a few aspects to note regarding the data. First, the highest reported specific capacitance value is collected for each nanostructure. Second, the area-normalized capacitance values are calculated with the same method as used for our results in Table 1, unless the values are reported in the article. Lastly, if the pore size is not reported as a single value but in a range, the largest dimension is listed as the pore size.

Table S6. Gravimetric power and energy densities characterized at current densities of 1, 2, 3, 4, 5, 10, and 20 A g⁻¹

Samples	Gravimetric Power Density [kW Kg⁻¹]							Gravimetric Energy Density [Wh Kg⁻¹]						
	$1\,A\,g^{-1}$	$2\,A\,g^{-1}$	$3\,A\,g^{-1}$	$4\,A\,g^{-1}$	$5\,A\,g^{-1}$	$10\,A\,g^{-1}$	$20\,A\,g^{-1}$	$1\,A\,g^{-1}$	$2\,A\,g^{-1}$	$3\,A\,g^{-1}$	$4\,A\,g^{-1}$	$5\,A\,g^{-1}$	$10\,A\,g^{-1}$	$20\,A\,g^{-1}$
SVP-30	2.4	4.89	7.12	9.42	11.74	22.44	39.94	32.98	28.3	26.21	25.21	24.53	22	18.64
SVP-50	2.41	4.86	7.43	9.83	12.22	24.84	48	37.5	34.03	33.11	31.7	30.59	28.01	24.27
SVP-70	2.13	4.45	6.7	8.96	11.15	23.92	55.26	45.81	42.12	40.78	39.63	38.34	35.55	32.23
SVP-100	2.93	5.91	8.98	12.13	14.76	31.07	61.8	40.28	37.86	37.08	36.45	34.49	33.4	30.9

Table S7. Volumetric power and energy densities characterized at current densities of 1, 2, 3, 4, 5, 10, and 20 A g⁻¹

Samples	Volumetric Power Density [kW L⁻¹]							Volumetric Energy Density [Wh L⁻¹]						
	$1\,A\,g^{-1}$	$2\,A\,g^{-1}$	$3\,A\,g^{-1}$	$4\,A\,g^{-1}$	$5\,A\,g^{-1}$	$10\,A\,g^{-1}$	$20\,A\,g^{-1}$	$1\,A\,g^{-1}$	$2\,A\,g^{-1}$	$3\,A\,g^{-1}$	$4\,A\,g^{-1}$	$5\,A\,g^{-1}$	$10\,A\,g^{-1}$	$20\,A\,g^{-1}$
SVP-30	1.10	2.23	3.25	4.30	5.37	10.26	18.26	15.08	12.93	11.98	11.53	11.21	10.06	8.52
SVP-50	1.09	2.19	3.36	4.44	5.52	11.22	21.69	16.94	15.37	14.96	14.32	13.82	12.65	10.96
SVP-70	0.96	2.00	3.01	4.03	5.01	10.75	24.84	20.59	18.93	18.33	17.81	17.23	15.98	14.49
SVP-100	1.31	2.64	4.02	5.43	6.61	13.90	27.65	18.02	16.94	16.59	16.31	15.43	14.94	13.83
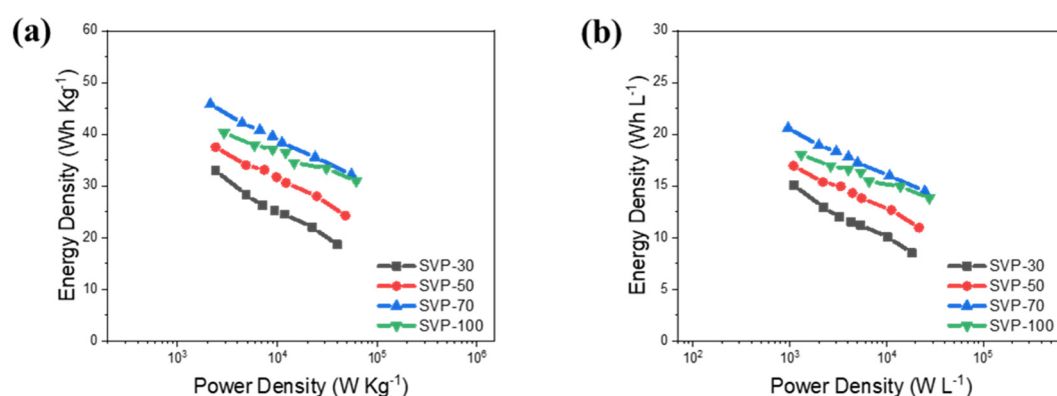
Figure S10. Ragone plot displaying (a) gravimetric and (b) volumetric energy and power densities of the electrodes.

The Ragone plot in Figure S10 compares the energy and power densities measured with GCD curves characterized at current densities of 1, 2, 3, 4, 5, 10, and 20 A g^{-1}. Parallel to the specific capacitance values in Figure 3c, the SVP-70 electrode shows the largest energy density values, followed by SVP-100, SVP-50, and SVP-30. As can be seen in the graphs, the energy densities of SVP-100 verges on those of SVP-70 at higher power densities, owing to the high rate capabilities allowing superior energy density retention under large current densities. Furthermore, electrodes with larger dimensions exhibit superior power densities, which is attributed to the enhanced electrolyte ion kinetics within the macro-channels.

References

1   T. Jawhari, A. Roid and J. Casado, *Carbon*, 1995, **33**, 1561–1565.

2   A. Yoshida, Y. Kaburagi and Y. Hishiyama, *Carbon*, 2006, **44**, 2333–2335.

3   R. Tang, K. Taguchi, H. Nishihara, T. Ishii, E. Morallón, D. Cazorla-Amorós, T. Asada, N. Kobayashi, Y. Muramatsu and T. Kyotani, *J. Mater. Chem. A*, 2019, **7**, 7480–7488.

4   L. G. Cançado, K. Takai, T. Enoki, M. Endo, Y. A. Kim, H. Mizusaki, A. Jorio, L. N. Coelho, R. Magalhães-Paniago and M. A. Pimenta, *Appl. Phys. Lett.*, 2006, **88**, 163106.

5   F. Tuinstra and J. L. Koenig, *J. Chem. Phys.*, 1970, **53**, 1126–1130.

6   S. Ardizzone, G. Fregonara and S. Trasatti, *Electrochim. Acta*, 1990, **35**, 263–267.

7   Z. Zhou, T. Liu, A. U. Khan and G. Liu, *Sci. Adv.*, , DOI:10.1126/sciadv.aau6852.

8   N. K. Sidhu and A. C. Rastogi, *Synth. Met.*, 2016, **219**, 1–10.

9   S. Ghosh, T. Mathews, B. Gupta, A. Das, N. Gopala Krishna and M. Kamruddin, *Nano-Structures & Nano-Objects*, 2017, **10**, 42–50.

10   M. Biswal, A. Banerjee, M. Deo and S. Ogale, *Energy Environ. Sci.*, 2013, **6**, 1249–1259.

11   B. Pandit, B. R. Sankapal and P. M. Koinkar, *Sci. Rep.*, 2019, **9**, 5892.

12   T. Purkait, G. Singh, D. Kumar, M. Singh and R. S. Dey, *Sci. Rep.*, 2018, **8**, 640.